Pacemaking function of two simplified cell models

Maxim Ryzhii[1,*], Elena Ryzhii[2]

1 University of Aizu, Complex Systems Modeling Laboratory, Aizu-Wakamatsu, Japan
2 Fukushima Medical University, Department of Anatomy and Histology, Fukushima, Japan

* m-ryzhii@u-aizu.ac.jp

Abstract

Simplified nonlinear models of biological cells are widely used in computational electrophysiology. The models reproduce qualitatively many of the characteristics of various organs, such as the heart, brain and intestine. In contrast to complex cellular ion-channel models, the simplified models usually contain a small number of variables and parameters which facilitates nonlinear analysis and reduces computational load. In this paper, we consider pacemaking variants of the Aliev-Panfilov and Corrado two-variable excitable cell models. We conducted numerical simulation study of these models, and investigated main nonlinear dynamic features of both isolated cells and 1D coupled pacemaker-excitable systems. Simulations of 2D sinoatrial node and 3D intestine tissue as application examples of combined pacemaker-excitable systems demonstrated results similar to obtained previously. The uniform formulation for the conventional excitable cell models and proposed pacemaker models allows a convenient and easy implementation for the construction of personalized physiological models, inverse tissue modeling, and development of real-time simulation systems for various organs that contain both pacemaker and excitable cells.

Introduction

Nowadays computer modeling of various organs and tissues is indispensable part of the physiology research. Computational models of different levels of complexity are being utilised, with complex ion-channel multi-variable models on the top of the list. A rigorous review of the cardiac models was presented in [1]. The number of such models and their updates increases yearly following new physiological findings and measurements. Consisting of many differential equations for ion channels and their gate formulations, the models provide detailed description of cell behavior under various normal and pathological conditions, including, for example, influence of drugs [2]. The number of variables and parameters in such models can reach several dozens, leading to the necessity to utilize significant computational resources, even despite of current progress in and availability of graphical processing units (GPU) and multicore processors [3]. Moreover, these precise ion-channel models, in particular, cardiac ones, usually require small enough time steps and mesh sizes to provide calculation stability, leading to hours and even days of calculation using normal desktop computers. Thus, utilization of the ion-channel based models in the simple systems, such as equipment test-beds and other real-time simulation devices and platforms, is still almost impossible.

In many cases a good alternative can be utilization of simplified phenomenological cell models, such as famous classical Van der Pol [4] (VDP), FitzHugh-Nagumo [5, 6]

Fig 1. Timeline of simplified physiological cell models development. Solid shapes correspond to excitable cell models, dashed shapes - to pacemaking cell models, respectively.

(FHN), and Hodgkin-Huxley [7] (HH) equations. These models are based on small number (usually $2-3$) of variables, i.e. ordinary differential equations (ODEs). Later additions to this class include modifications of the HH and FHN models, namely Van Capelle-Durrer (VCD) [8], Aliev-Panfilov [9] (AP), Morris-Lecar [10] and its pacemaking variants [11, 12], Fenton-Karma [13], Mitchell-Schaeffer [14] (MS), and its modification by Corrado and Niederer [15] (CN). Most of the above mentioned models are included into the modeling software packages and repositories, such as openCARP [16] and Physiome Project [1, 17].

Fig 1 demonstrates timeline of the historical development of main simple physiological models. Solid shapes correspond to the excitable models, dashed - to the pacemaking models, and the models capable to exhibit both types of behavior are represented by both shape types. Even though the majority of the models shown in Fig 1 is capable to provide pacemaking operation, their utilization is limited. The VDP and FHN models and their modifications are being predominantly used as simple models of natural pacemakers in physiological simulations of different levels of complexity (see, for example, [18–22]). The VDP model of relaxation oscillator was proposed to describe general heartbeat dynamics and by its nature does not have the quiescent excitable form. The two-variable FHN model, as a reduction of the four-variable HH model of the squid giant axon action potential, was developed to model neuronal excitability. It has the properties of producing spike trains (tonic spiking) at sufficiently large stimulating constant current, and the apparent absence of a firing threshold [23], which are undesirable for simulation of other organs, such as the heart.

The disadvantage of other simplified models simulating both pacemaker and non-pacemaker action potentials of cardiac cells like VCD, Morris-Lecar, and their modifications is the significant number of parameters that limits the areas of their utilization. On the other hand, computationally lightweight models such as AP, MS, and CN are being successfully used for solution of cardiac inverse problem and building patient-specific models [24–27]. The MS model, however, is known to have some stability problems [15].

For multi-scale and real-time simulations the models with modest number of parameters are preferable. Such models have been implemented in many studies of electrophysiology of the heart and cardiac tissue [28–32] as well as intestine [18, 33], stomach [34], uterus [35], and bladder [36]. Recently, the AP model was used in deep learning-based reduced order modeling [37], allowing to boost the solution of parameterized problems in cardiac electrophysiology.

Another recently proposed type of pacemaker models developed to satisfy real-time requirements is represented by parametric [38] and resonant [39] (8–24 variables) models. They quantitatively reproduce action potential shapes and some cellular behavior, but do not include several important physiological properties such as interactions due to electrotonic coupling. Although the models provide relatively low computational load, the latter may significantly rise with inclusion of the detailed features. The above mentioned models, however, underline the need for simple computationally efficient models, in particular, having unified description for pacemaking and excitable cells.

In this work, we consider variants of the AP and CN cellular models providing them intrinsic pacemaker properties (hereinafter called pAP and pCN, respectively), and demonstrate their main characteristics for both single pacemaking cells and coupled pacemaker-excitable systems.

As application examples for the proposed pacemaker models, we include simulations

of 2D cardiac sinoatrial node (SAN) model described with the pAP and AP cells, and 3D intestinal model consisting of the pCN and CN cells.

Methods

Self-oscillations in Aliev-Panfilov model

The two-variable AP model [9] proposed to describe non-oscillatory cardiac tissue that supports stable propagation of excitation waves is represented by the following set of reaction-diffusion type nonlinear ordinary differential equations:

$$\frac{\partial u}{\partial t} = c_t[ku(u-a)(1-u) - vu] + I_{ext}, \tag{1}$$

$$\frac{\partial v}{\partial t} = c_t\varepsilon[-v - ku(u-a-1)], \tag{2}$$

$$\varepsilon = \varepsilon_0 + \frac{v\mu_1}{u+\mu_2},$$

where u and v are normalized transmembrane potential and slow recovery variable, respectively. Parameter k controlling the magnitude of transmembrane current, and parameters μ_1, μ_2, and a are adjusted to reproduce characteristics of cardiac tissue, ε sets the time scale of the recovery process, $c_t = 1/12.9$ is the time scaling coefficient introducing physical time in milliseconds into the system. $I_{ext} = \nabla \cdot (\mathbf{D}\nabla u)$ is external or coupling current in the case of multi-cell simulations, where ∇ is a spatial gradient operator defined within the model tissue geometry, and $\mathbf{D}$ is a tensor of diffusion coefficients (in $\mathrm{mm}^2\mathrm{ms}^{-1}$) characterizing electrotonic interactions between neighbouring cells via gap junctional coupling conductance.

In the conventional AP model the left branch of the u-nullcline $v = k(u-a)(1-u)$ (dashed lines in Figs 2A.1 and 2A.2) does not enter the region where u is negative. The phase space trajectory (shown after suprathreshold stimulation in Fig 2A.1) is also limited in the region $u > 0$ by the second u-nullcline $u = 0$.

As the excitation threshold a reduces, the nullcline moves up, its left branch moves toward $u < 0$. When the parameter a becomes negative, the u-nullcline intersects the v-nullcline $v = -ku(u-a-1)$ (dotted lines in Figs 2A.1 and 2A.2) creating equilibrium points (EP) in the $u > 0$ region. The system of Eqs (1–2) undergoes Hopf bifurcation (HB), which is a typical mechanism for the onset of oscillations with a stable limit cycle (periodic orbit) in nonlinear dynamical systems [40]. For the sake of convenience, further we introduced a parameter $b_{AP} = -a$ in Eq (1), controlling the intrinsic oscillation frequency when $b_{AP} > 0$:

$$\frac{\partial u}{\partial t} = c_t[ku(u+b_{AP})(1-u) - vu] + I_{ext}\,. \tag{3}$$

The idea to use of the parameter b_{AP} for cubic u-nullcline in the FHN-like systems to control excitability range is straightforward. It has been used, for example, to study the propagation of action potential in combined pacemaking-excitable FHN model tissue [41]. However, in the case of the AP model, which was developed primarily to represent excitable cardiac tissue, the intrinsic pacemaking function in a single cell and coupled systems was not considered yet.

The resulting phase space geometry of the pAP model is shown in Fig 2A.2. Three stable limit cycles with $b_{AP} = 0.01$, 0.03, and 0.05 and their EPs (marked by squares) in Fig 2A.2.

Corrado excitable cell model and its pacemaking variant

The two-variable CN modification [15] of the ionic MS model [14] for cardiac excitable cells is represented by the following set of nonlinear differential equations:

$$\frac{\partial u}{\partial t} = \frac{hu(u-u_{gate})(1-u)}{\tau_{in}} - \frac{(1-h)u}{\tau_{out}} + I_{ext}, \tag{4}$$

$$\frac{\partial h}{\partial t} = \begin{cases} \frac{1-h}{\tau_{open}} & \text{if } u \le u_{gate} \\ \frac{-h}{\tau_{close}} & \text{if } u > u_{gate} \end{cases}. \tag{5}$$

Here h is the gate variable for the inward current (sodium ion channels), $u_{gate} > 0$ is the excitation threshold potential, τ_{in}, τ_{out}, τ_{open}, and τ_{close} are the time constants affecting the corresponding characteristic phases of the evolution of transmembrane potential u (shown after suprathreshold stimulation in Fig 2B.1). As in the pAP model, the latter is also limited in the region $u > 0$ by the second u-nullcline $u = 0$.

To introduce pacemaking behavior into the CN model, we did the following modifications. First, the piece-wise function (Eq 5) was replaced by the formulation with sigmoid function [7, 42] of the transmembrane potential (Eqs 7–9) with the slope factor u_s (in dimensionless voltage units), similar to the approach used in [43], changing the shape of h-nullcline [44]. Second, we replaced u_{gate} in Eq 4 by a parameter $b_{CN} = -u_{gate}$, allowing to shift independently left branch of the u-nullcline $h = \tau_{in}/[\tau_{out}(u-u_{gate})(1-u)+\tau_{in}]$:

$$\frac{\partial u}{\partial t} = \frac{hu(u+b_{CN})(1-u)}{\tau_{in}} - \frac{(1-h)u}{\tau_{out}} + I_{ext}, \tag{6}$$

$$\frac{\partial h}{\partial t} = \frac{(h_\infty - h)}{\tau}, \tag{7}$$

$$\tau = \frac{\tau_{open}\tau_{close}}{\tau_{open} - h_\infty(\tau_{close} - \tau_{open})} \tag{8}$$

$$h_\infty = \frac{1}{2}\left[1 - \tanh\left(\frac{u-u_{gate}}{u_s}\right)\right]. \tag{9}$$

Similar to the pAP model, b_{CN} becomes a parameter suitable for control both the CN cell excitability and the pCN intrinsic oscillation frequency (see Fig. 5A.1 below).

Replacement of the Heaviside-like step function in Eq 5 for h_∞ by the sigmoid voltage dependence in the limit [42] (conventional Boltzmann equation for cell membranes [7])

$$H(x) = \lim_{u_s \to 0}\left(1 + \exp\left(-\frac{x}{u_s}\right)\right)^{-1} = \frac{1}{2}\lim_{u_s \to 0}\left[1 - \tanh\left(-\frac{x}{u_s}\right)\right]$$

and the increase of the slope factor u_s reduce the robustness of the CN model and enhance its propensity to spontaneous oscillations by inclination the central branch of the h-nullcline (dotted lines in Figs 2B.1 and 2B.2). This, together with the shift of the left branch of the u-nullcline (dashed lines in Figs 2B.1 and 2B.2) toward $u < 0$ region with increasing parameter b_{CN}, leads the system of Eqs 6–7 to HB, creates EP at the nullclines intersection, and provides the appearance of a stable limit cycle. The parameters u_s and u_{gate} together with b_{CN} define the position of u and h nullclines intersection, and consequently the shape of phase space trajectory (see Figs 5A.1, 5B.1, and 5C.1 below).

Though the method is similar to the previously proposed pacemaking modification of the MS excitable cell model [43], the considered pCN model (Eqs 6–9) possesses different nonlinear dynamic properties.

Fig 2. Single cell nonlinear dynamics. **A: AP and pAP models**. A.1: Nullclines and phase portrait for the conventional AP model after suprathreshold stimulation. A.2: Nullclines and phase portrait for the pAP model with different bifurcation parameter b_{AP}. Dashed and dotted lines correspond to u- and v-nullclines, respectively. Nullcline $u = 0$ is not shown. Stable limit cycles for $b_{AP} = 0.01$, 0.03, and 0.05 are shown with corresponding EPs marked by squares of the same color. A.3: Action potentials, colors correspond to the curves in (A.2). **B: CN and pCN models**. B.1: Nullclines and phase portrait for the conventional CN model after suprathreshold stimulation. B.2: Nullclines and phase portrait for the pCN model with different bifurcation parameter b_{CN}. Dashed and dotted lines correspond to u- and h-nullclines, respectively. Nullcline $u = 0$ is not shown. Stable limit cycles for $b_{CN} = 0.12$, 0.3, and 0.44 are shown with corresponding EPs marked by squares of the same color. B.3: Action potentials, colors correspond to the curves in (B.2).

Note the clockwise direction with respect to the second variable in the limit cycles of the pCN model (Figs 2B.1 and 2B.2) in contrast to the pAP model (Figs 2A.1 and 2A.2).

Isolated single pacemaker cells

For single-cell cases (0D), we examined dynamics of the pAP and pCN model cells changing various bifurcation parameters and constructing bifurcation diagrams [45]. The incremental steps of the parameters were selected individually for each model, and varied depending on observed dynamics. When spontaneous oscillation appeared, we determined peak overshoot potential (POP), maximum diastolic potential (MDP), frequency, diastolic interval (DI) and AP duration at 90% repolarisation (APD) for each bifurcation parameter value upon allowing the oscillation activity to stabilize within 20 – 50 s.

Coupled 1D pacemaker-excitable systems

One of the important characteristics of a pacemaking cell is its synchronization behavior under applied load of coupled cells with variable diffusion coefficient. To investigate this characteristic for the considered pacemaking cells we set up three variants of the load - n strands (cables) of matching 20 excitable cells coupled to a single pacemaker cell. Because the load in a tissue is not limited to an integer value (n can be non-integer [46]), apart from normal case ($n = 1$) we considered higher ($n = 2$) and lower ($n = 0.5$) loads.

Minimal and maximal frequencies of complete 1:1 synchronization

In a wide range of fixed values of the coupling coefficient $d = D/\Delta x^2 = 0.02 - 10.0$ ms^{-1} (D is the diffusion coefficient) we run multiple simulations of the pAP-AP and pCN-CN coupled systems, varying the values of the control parameters b_{AP} and b_{CN}, respectively, calculating the resulting frequency ratio between the pacemaker cell and the 16th excitable cell in a strand (to eliminated possible effects of the boundary conditions on the last cell). Next we determine the lowest (minimal) and highest (maximal) frequency of the system with complete 1:1 synchronization between the cells.

Relationship between pacemaker cell rates and intercellular coupling

In these simulations we fixed intrinsic oscillation frequency of the pacemaker cells (fixing the parameters b_{AP} and b_{CN}) at the values close to upper frequency limit of 1:1 pacemaker-excitable system synchronization. Changing the intercellular coupling d we examined the onset of transitions between full 1:1 and incomplete synchronizations (similar to Fig 12 in [47]), and recorded obtained frequencies of the pacemaking cell and the 16th excitable cell in the strand.

Fig 3. Schematics of the simulation examples. A: 2D SAN model with the pAP-AP cells. B: 3D intestine model with the pCN-CN cells.

2D SAN model

The primary natural cardiac pacemaker, SAN, consists of a small area of specialized cells that are situated in the right atrium (the right upper chamber of the heart). The SAN dysfunctions may result in dangerous cardiac arrhythmias. The mechanisms and processes involved in the latter are very complicated and may be difficult or nearly impossible to explain without the help of computer modeling.

As an application example for the pAP-AP system we replicated simplified 2D SAN simulation model used to illustrate the effect of SAN - atrium coupling on the pacemaking behavior (Fig 11 in [47]). The model consists of a rectangular area 10 mm by 10 mm (200×200 mesh, $\Delta x = 0.05$ mm spatial step size) of atrial tissue represented by AP model cells (Fig 3A). The whole 2D model is anisotropic with the ratio of diffusion coefficients $D_y : D_x = 1{:}0.208$ ($1.2 : 0.25$ conductivity ratio in [47]) along the fiber longitudinal y and transverse x directions, respectively. The pacemaker was defined as an elliptically shaped area of pAP cells in the center of the rectangular with half-axes 3 and 1 mm, and long SAN axes 30° off the fiber direction. Three different values of diffusion coefficient $D_y = 0.120$, 0.060, and 0.048 $\mathrm{mm^2ms^{-1}}$ were used. In this simple SAN structure we did not incorporate neither diffusion gradients nor electrical heterogeneity of pacemaker cells, in contrast to widely adopted approach in the simulations with ion-channel models [48, 49].

3D intestine model

There are two main layers of different cell types in the intestine. The first layer of specialized pacemaker cells, termed interstitial cells of Cajal (ICC), produces slow propagating electrical waves. The ICC synchronize to the highest frequency within the layer. This electric activity of the ICC controls the contractile stress exerted by second layer of the smooth muscle cells (SMC) of the intestinal tissue. The both layers of ICC and SMC are electrically connected via electrotonic coupling.

In the second application example for the proposed pacemaker models, we considered a simple 3D elecrophysiological model of the small intestine. As a reference, we took some of the results from the papers [18, 33], in which the MS and FHN models were used. In contrast to the works, we described ICC and SMC layers with the pCN and CN model cells, respectively, to demonstrate the broad applicability of the pCN model. It has been demonstrated that the excitable MS model is apt to spontaneous excitations at some conditions, with its modification proved to be robust to such pacemaker behavior [15]. Using the pCN model with improved frequency control in the combination with robust CN model instead of the MS and FHN models may improve the behavior of the pertinent computational tissue models.

Similar to [18, 33], our intestine model geometry is presented by a long two-layer tube, cut along its axle y on one side and stretched to a dual-layer plane (Fig 3B). The blue and red surfaces in Fig 3B represent external SMC and internal ICC layers, respectively. Such a simple tube geometry corresponds to anatomy of the small intestine in general. The simulation domain for both layers has dimensions $N_x \times N_y = 252 \times 2400$, with uniform spatial mesh size $\Delta x = 0.5$ mm, which corresponds to the 1200 mm long tube (one half of that in [18]) with the mean circumference of 126 mm (40 mm diameter).

Electrical dynamics in the intestine layers is described by the following set of ODEs

for transmembrane potentials u^{I} of ICC and u^{M} for SMC:

$$\frac{\partial u^{\mathrm{I}}}{\partial t} = I^{\mathrm{I}}_{tot} + D^{\mathrm{IM}}(u^{\mathrm{M}} - u^{\mathrm{I}}), \tag{10}$$

$$\frac{\partial u^{\mathrm{M}}}{\partial t} = I^{\mathrm{M}}_{tot} + D^{\mathrm{IM}}(u^{\mathrm{I}} - u^{\mathrm{M}}), \tag{11}$$

where I^{I}_{tot} and I^{M}_{tot} represent right-hand side of the Eq 6 for ICC and SMC layers, respectively, and last terms in the right-hand side of Eq 10 and 11 describe electrotonic coupling between the layers with diffusion coefficient $D^{\mathrm{IM}} = 0.006$ mm^{2}ms^{-1}. Conduction within the layers was considered isotropic with the diffusion coefficients $D^{\mathrm{I}} = 0.0012$ and $D^{\mathrm{M}} = 0.012$ mm^{2}ms^{-1} for the ICC and SMC, respectively. Each of Eq 10 and 11 is accompanied by the three corresponding equations for slow currents h^{I} and h^{M} similar to Eqs 7–9.

Individual isolated ICC oscillate at different intrinsic frequencies, with spatial frequency gradient in the longitudinal direction from the pylorus (first part of duodenum, left side in Fig 3B) toward ileum (right side in Fig 3B). To create the frequency gradient in the ICC layer, for Eq 10 we set up a linear distribution of the parameter b_{CN} along y axis (and constant along x axis):

$$b_{CN}(i) = b^{\max}_{CN} - (b^{\max}_{CN} - b^{\min}_{CN})\frac{i-1}{N_y},\ i = 1...N_y \tag{12}$$

where i is the cell index counting from the duodenum.

To demonstrate appearance of intestinal dysrhythmias in a similar way as in [33], the conduction block ($u^{\mathrm{I}} = u^{\mathrm{M}} = 0.002$, $h^{\mathrm{I}} = h^{\mathrm{M}} = 0.005$) was applied at $t = 150$ s to the rectangular area at both ICC and SMC layers with the width $l_y = 250$ mm, height $l_x = 63$ mm, and origin at $x_0 = 0$ and $y_0 = 475$ mm. Neither the electromechanical [33] nor thermodynamical [18] coupling was included in the model for the sake of simplicity.

Numerical methods

All simulations were performed with MATLAB (R2021a). Explicit forward Euler (fE) method of integration with space and time steps was used to solve the ODEs. No-flux Neumann boundary conditions were applied in 1D, 2D, and 3D simulations with exception to the periodic boundary conditions along y axes in the 3D intestine model. Equilibrium points for bifurcation diagrams were calculated with MatCont software [50]. The parameters for the AP and pAP, CN and pCN models used in the simulations are listed in Table 1 and Table 2, respectively. The initial conditions for the models were chosen to be $u(0) = 0.01$, $v(0) = 0.01$ for the AP and pAP, and $u(0) = 0.01$, $h(0) = 0.2$ for the CN and pCN models.

The accuracy of the results for single cell simulations with fE method at different time steps Δt were compared with that calculated with unconditionally stable implicit backward Euler (bE) method with small time step $\Delta t = 0.0001$ ms. The relative norms

$$L_2 = \frac{\parallel u^{\mathrm{bE}} - u^{\mathrm{fE}} \parallel_2}{\parallel u^{\mathrm{bE}} \parallel_2} \text{ and } L_\infty = \frac{\parallel u^{\mathrm{bE}} - u^{\mathrm{fE}} \parallel_\infty}{\parallel u^{\mathrm{bE}} \parallel_\infty}$$

(for a single cycle) and relative frequency error (for 60 s runs), as well as speedup of calculations are given in Table 3. For 1D coupled pacemaker-excitable systems the maximum relative frequency error with $\Delta t = 0.1$ ms was also about 0.16%. As seen from Table 3, in most cases of the simulations with the pAP and pCN models the fE method with time step of 0.1 ms would be enough to obtain reasonable accuracy. This

Table 1. Parameters for AP and pAP models in the 0D (isolated cell), 1D, and 2D simulations.

Cell	k	a	ε_0	μ_1	μ_2	b_{AP}	Δt (ms)
pAP (0D)	8	0.13	0.002	0.2	0.3	0 – 0.08	0.01
pAP (1D)						0 – 0.5	0.1 – 0.01
AP (1D)						-0.13	
pAP (Sinus node)					0.5	0.12	0.005
AP (Atrial tissue)			0.045		0.3	-0.13	

Table 2. Parameters for CN and pCN models in the 0D (isolated cell), 1D, and 3D simulations.

Cell	τ_{in} (ms)	τ_{out} (ms)	τ_{open} (ms)	τ_{close} (ms)	u_s	u_{gate}	b_{CN}	Δt (ms)
pCN (0D)	0.3	6.0	120	150	0.05 – 0.55	-0.1 – 0.35	0.05 – 0.6	0.01
pCN (1D)					0.15	-0.05	0.1 – 12	0.1 – 0.01
CN (1D)					0.01	0.13	-0.13	
pCN (ICC)	3.4	47	1500	2500	0.30	-0.05	0.16/0.22	0.5
CN (SMC)	4.5				0.01	0.13	-0.13	

Table 3. Comparison of the accuracy of simulation results with different time step Δt.

Cell	**fE**, $\Delta t = 0.1$ ms				**fE**, $\Delta t = 0.01$ ms				**fE**, $\Delta t = 0.001$ ms			
	L_2	L_∞	Freq.	Speedup	L_2	L_∞	Freq.	Speedup	L_2	L_∞	Freq.	Speedup
pAP	0.25%	0.93%	0.17%	707	0.14%	0.38%	0.017%	218	0.01%	0.01%	0.002%	36
pCN	0.53%	2.03%	0.16%	1040	0.13%	0.45%	0.016%	123	0.08%	0.28%	0.002%	14

may be especially useful for whole-organ simulations where the computation time is a critical factor. At the same time, the standard stability criterion

$$\frac{D\Delta t}{\Delta x^2} = d\Delta t < \frac{1}{2N},$$

where N is the dimension of the simulation domain, should be taken into account as well [51].

Results and discussion

Single-cell pacemaker dynamics

The phase portraits and nullclines of excitable and pacemaking model variants are presented in Fig 2. Three action potential waveforms are demonstrated in Figs 2A.3 and 2B.3. They correspond to the limit cycles with EPs shown by squires of the same color in Figs 2A.2 and 2B.2, calculated with different values of the parameters b_{AP} and b_{CN}, respectively.

Absence of the undershoot of the action potential amplitude in the pAP and pCN models (in contrast to the FHN model [5,6]) makes them specifically suitable for utilization as secondary pacemakers and in the cardiac simulation systems with limited number of elements, similar to proposed in the works [38,39,52].

Figs 4 and 5 demonstrate dependence of single cell dynamic characteristics of the pAP and pCN models on various bifurcation parameters. The trajectories of the EPs are shown by dashed lines in the left columns of Figs 4 and 5.

All the bifurcation parameters affect the intrinsic oscillation frequency (central columns of Fig 4 and Fig 5). For pAP the highest variation in the frequency was observed with b_{AP} (with almost linear dependency, Fig 4A.2) and I_{ext} (Fig 4E.2). The

Fig 4. Dependence of pAP cell characteristics on various parameters. A: on the bifurcation parameter b_{AP}, B: on the parameter ϵ_0, C: on the parameter μ_1, D: on the parameter μ_2, E: on the external current I_{ext}. Left panels correspond to the bifurcation diagrams, central - to the calculated frequencies, and right panels - to the calculated DI on APD ratios.

Fig 5. Dependence of pCN cell characteristics on various parameters. A: on the bifurcation parameter b_{CN}, B: on the slope factor u_s, C: on the parameter u_{gate}, D: on the external current I_{ext}. Left panels correspond to the bifurcation diagrams, central - to the calculated frequencies, and right panels - to the calculated DI on APD ratios.

former allows most convenient control of the frequency, while the latter indicates strong sensitivity of the model to the external coupling strength. The variation of POP and MDP is strongest also for b_{AP} and I_{ext}. The increase of the parameter μ_2 in the $0.1 - 0.5$ range decreases of the frequency, and higher values of μ_2 seem to be impractical (Fig 4D.2). For the pCN model significant variation of POP and MDP was observed for all bifurcation parameters (left columns in Fig 5).

The dependencies of DI/APD ratios on the bifurcation parameters are shown in the right columns of Figs 4 and 5. The ratios supplement the intrinsic frequency characteristics demonstrating DI and APD contributions into the cycle length. With decreasing DI/APD ratio steepness of the restitution curve (APD on DI) increases. At some combination of the parameters the ratios are always higher than unity (see, for example, $b_{AP} = 0.005$ curve in Fig 4C.3). For the pCN model this takes place only for I_{ext} dependence (Fig 5D.3).

In the pCN model b_{CN} (Fig 5A.2) and u_{gate} (Fig 5C.2) are the parameters with the highest variation of intrinsic frequency. The parameter b_{CN}, similar to b_{AP}, allows to obtain very low oscillation rates (less than 0.1 Hz). The influence of I_{ext} (Fig 5D.2) on the frequency is relatively weak, thus the pCN model looks less sensitive to the coupling strength (compare with Fig 4E.2, see also Fig 6).

Both models demonstrated notably wide range of intrinsic frequencies: $0.007 - 7.6$ Hz for pAP, $0.14 - 14$ Hz for pCN, corresponding to about $0.4 - 450$ and $8.4 - 840$ counts per minute (cpm), respectively. Such a broad frequency span allows implementation of the models for simulation of various organs of different animal species at normal and pathological conditions.

For the pCN model, the frequency and, in particular, DI/APD ratios depend also on the time constants τ_{in}, τ_{out},τ_{open}, and τ_{close}. The influence of the constants on pCN characteristics is similar to that for the original and modified MS models [14, 15, 43].

Dynamics of 1D coupled pacemaker-excitable system

Depending on the coupling (diffusion coefficient) the pacemaker-excitable system may be either in a fully synchronized (1:1) regime, when all excitable cells in a strand follow the driving frequency, or in a asynchronous/chaotic regime, when not all of the pacemaker action potentials are able to propagate to the end of the strand [47, 53].

Figs 6A.1 and 6B.1 demonstrate dependencies of minimal and maximal frequencies of complete 1:1 synchronization and corresponding minimal and maximal values of parameters b_{AP} and b_{CN} on the coupling coefficient $d = D/\Delta x^2$ for the single pAP and pCN model cells coupled with $n = 0.5$, 1, 2 strands of 20 AP and CN excitable cells, respectively.

For the pAP-AP coupled system, the complete synchronization was confined in two separate areas created by interlocks of minimal and maximal frequency curves (Fig 6A.1). The areas partially merged in the case of $n = 0.5$. Similar corresponding separate areas of the parameter b_{AP} are seen in Fig 6A.2. This indicates that at certain values of d complete 1:1 synchronization in the pAP-AP system with heavy load can not

Fig 6. A: 1D pAP-AP coupled system. (A.1) Minimal and maximal 1:1 synchronized frequency dependence on the coupling coefficient d for the pAP cell coupled with $n = 2$ (red), 1 (green), and 0.5 (blues) strands of 20 AP cells. Inset illustrates schematic representation of the 1D pAP-AP coupled system. Ellipse symbolizes pacemaker cell, and rectangles - excitable cells. (A.2) Minimal and maximal values of the parameter b_{AP} vs d corresponding to panel (A.1).
B: 1D pCN-CN coupled system. (B.1) Minimal and maximal 1:1 synchronized frequency dependence on the coupling coefficient d for the pCN cell coupled with $n = 2$ (red), 1 (green), and 0.5 (blue) strands of 20 CN cells. Inset illustrates schematic representation of the 1D pCN-CN coupled system. (B.2) Minimal and maximal values of the parameter b_{CN} vs d corresponding to panel (B.1).

Fig 7. Synchronization in the simplified 1D coupled model systems with fixed parameters *b*. Dependence of synchronization in the pAP-AP (A) and pCN-CN (B) systems with different number of excitable cell strands n on the coupling parameter d. Solid lines correspond to the pacemaker frequency, and the dotted lines - to the frequency at the 16th excitable cell in the strand(s).

be obtained at least with the model parameters used.

The existence of the two separate areas in the coupling dependence characteristics is associated with two possible variants of intersections between branches of the parabolic nullclines of the pAP model (Eqs 2 and 3). The areas of complete synchronization became smaller with increasing number of stands n.

We also observed a pronounced hysteresis in the case with $n = 0.5$ (and a very small one in the case with $n = 1.0$) of the maximal synchronized frequency characteristic at low coupling strength. Such effect seems to be similar to that demonstrated in the simulations of electrically coupled pacemaker and non-pacemaker cells with the VCD model [54].

In the pCN-CN coupled system, changes in the complete synchronization areas for different n were insignificant, and maximal synchronized frequency monotonically increased (Fig 6B.1). Figs 6B.1 and 6B.2 demonstrate much wider synchronization areas for both frequency and parameter b_{CN}. This may be attributed to higher energy capacity of the pCN over pAP cell with conventional model parameters. For both models increasing number of strands and increasing coupling strength required rising values of corresponding parameter b to maintain complete synchronization (Figs 6A.2 and 6B.2).

Synchronization behavior with fixed intrinsic pacemaker frequency

Fig 7 demonstrates synchronization behavior of the pAP-AP and pCN-CN 1D systems with increasing coupling at fixed bifurcation parameters (fixed intrinsic pacemaker frequency). One can observe in Fig 7 the presence of a certain threshold value of the coupling coefficient d, below which the pacemaker frequency was much higher than that of the coupled strand(s) of excitable cells. With the reduction of d from the threshold value the pacemaker-excitable frequency ratios increased significantly with abrupt jumps as observed in most of the simulated cases. The threshold values decreased with increasing coupling load, i.e. with increasing number of strands n. Above the threshold values of d complete synchronization occurred with smooth gradual drop of the frequency in the pAP-AP system (Fig 7A), while in the pCN-CN system it reaches a maximum before final fall-off (Fig 7B).

Fig 8. 2D simulation of SAN. Calculated time sequences of the transmembrane potential u along the bold black line in Fig 3A for different diffusion coefficients D. A: $D = 0.120$ mm^{2}ms^{-1}. B: $D = 0.060$ mm^{2}ms^{-1}. C: $D = 0.048$ mm^{2}ms^{-1}.

Fig 9. 3D simulation of intestine. Snapshots of spatial distributions of the transmembrane potential u^{I} in the ICC layer at different time moments t demonstrating gastric dysrhythmia (spiral) patterns due to conduction block applied at $t = 150$ s to both ICC and SMC layers.

2D simulation of SAN

Fig 8 shows the calculated spatio-temporal distributions of the transmembrane potential u from the central SAN region to peripheral atrial tissue (along the bold black line in Fig 3A) for different diffusion coefficients D. With relatively strong coupling ($D = 0.120$ mm^{2}ms^{-1}) SAN and atrial excitations were synchronized with slow pacing rate (about 55 cycles per minute, Fig 8A, see also S1 Video). At the reduced coupling strength ($D = 0.060$ mm^{2}ms^{-1}) the synchronization still persisted at the higher pacing rate (about 200 cpm, Fig 8B and S2 Video). When the coupling became too weak ($D = 0.048$ mm^{2}ms^{-1}), the atrial tissue failed to respond on every SAN excitation with 2:5 ratio (Fig 8C, S3 Video). The simulation results of this example are close to that demonstrated previously with the similar 2D SAN structure using complex ion-channel cell models with sufficient and weak SAN-atrial coupling (see Fig 11 in [47]).

Additional simulated variants with strong coupling but higher intrinsic frequency of the pAP pacemakers ($b_{AP} = 0.13$ and 0.18) are demonstrated in supplementing S4 Video and S5 Video.

3D simulation of intestine

The results of the 3D intestine simulations are presented in Fig 9 (see also the animated version in S6 Video). The figure shows spatial distributions of the transmembrane potential u^{I} in the ICC layer at different moments.

After beginning of the simulation, the potential waves initiated by the fastest pacemaker (on the left side, at $y = 0$) propagated rightward. The velocity and width of the action potentials gradually decreased in this direction (topmost panel in Fig 9) due to initial gradient of intrinsic frequencies in the ICC layer (Eq 12). At about $t = 140$ s a full entrainment of the system occurred, resulting in the constant velocity and width of the action potentials (second panel in Fig 9). The third panel in Fig 9 demonstrates the situation right upon the application of the conduction block ($t = 150$ s). The block overlapped two consequent pulses, thus initiating two similar perturbations. After $t = 165$ s (fourth panel), two spiral waves were formed, sending excitation waves with short period in both directions. These waves by secondary sources gradually superseded the original pulse waves initiated in the ICC layer (fifth panel), resulting in the full suppression of the latter ones (bottom panel). The action potentials in the SMC layer followed the ones in the ICC layer with small time shift and difference in shape (not shown). This intestinal dysrhythmia generally corresponds to that demonstrated in the previous simulations with the FHN (Fig 5 in [18]) and MS (Fig 7 in [33]) models.

General remarks

Though both the original AP and CN models were introduced to describe the cardiac action potential, they have been also utilized for simulations of various organs which contain both pacemaking and excitable cells. We intentionally did not try to tune precisely the parameters of the pAP and AP cells to the existing experimental SAN and atrial tissue data (including the shape of action potentials), with the aim just to

demonstrate the applicability of the pAP model for simulations of complex physiological configurations. Additional tuning of the parameters might be necessary for accurate simulation of organs other than the heart, as seen from the case of the 3D intestine model.

The utilization of the considered pacemaker models can be beneficial for the development of simplified real-time simulation systems (e.g. personalized medicine [24, 25] and inverse cardiac modeling [26]), deep learning [37], as well as for medical device testing platforms [38, 52].

Conclusion

In this work, we consider pacemaking variants of the Aliev-Panfilov and Corrado two-variable excitable cell models. We studied main features of single cell nonlinear dynamics of the models, their synchronization behavior in one-dimensional coupled pacemaker-excitable setups, including regions of complete 1:1 synchronization, and relationship between pacemaker frequency and overall coupling.

Also, we performed simulations of simplified 2D SAN and 3D intestine models employing the proposed pacemakers. The obtained spatio-temporal dynamics of the transmembrane potentials in the 2D and 3D models is in general agreement with that demonstrated previously for identical schematics with different cell models.

One of the important features of the considered pacemaker models is that they do not include neither any additional expression for currents nor additional ODE, thus having the same number of variables as the original excitable models. We believe that our proposed models can be effectively used for computationally efficient electrophysiological modeling of tissues that include primary and subsidiary pacemaking cells, allowing to build different models of whole organs with simple uniform model description, as well as for patient-specific medicine and medical device testing requiring real-time simulations.

Supporting information

S1 Video. Simulation of SAN. Animation of the transmembrane potential u in the SAN model structure with $D = 0.120$ mm^{2}ms^{-1}. (MP4)

S2 Video. Simulation of SAN. Animation of the transmembrane potential u in the SAN model structure with $D = 0.060$ mm^{2}ms^{-1}. (MP4)

S3 Video. Simulation of SAN. Animation of the transmembrane potential u in the SAN model structure with $D = 0.048$ mm^{2}ms^{-1}. (MP4)

S4 Video. Simulation of SAN. Animation of the transmembrane potential u in the SAN model structure with strong coupling ($D = 0.120$ mm^{2}ms^{-1}) and $b_{AP} = 0.13$ (about 90 cpm). (MP4)

S5 Video. Simulation of SAN. Animation of the transmembrane potential u in the SAN model structure with strong coupling ($D = 0.120$ mm^{2}ms^{-1}) and $b_{AP} = 0.18$ (about 300 cpm). (MP4)

S6 Video. Simulation of intestine. Animation of the transmembrane potential u^{I} in the intestine model. (MP4)

References

1. Noble D, Garny A, Noble PJ. How the Hodgkin–Huxley equations inspired the Cardiac Physiome Project. J Physiol. 2012; 590: 2613–2628. https://doi.org/10.1113/jphysiol.2011.224238

2. Niederer SA, Lumens J, Trayanova NA. Computational models in cardiology. Nat Rev Cardiol. 2019; 16: 100–111. https://doi.org/10.1038/s41569-018-0104-y

3. Niederer S, Mitchell L, Smith N, and Plank G. (2011) Simulating human cardiac electrophysiology on clinical time-scales. Front Physiol. 2011; 2: 14. https://doi.org/10.3389/fphys.2011.00014

4. Van der Pol B, van der Mark J. The heartbeat considered as a relaxation oscillation and an electrical model of the heart. Philosophical Magazine 1928; 6: 763–775. https://doi.org/10.1080/14786441108564652

5. FitzHugh R. Impulses and physiological states in theoretical models of nerve membrane. Biophys J. 1961; 1: 445–466. https://doi.org/10.1016/S0006-3495(61)86902-6

6. Nagumo J, Arimoto S, Yoshizawa S. An active pulse transmission line simulating nerve axon. Proc IRE. 1962; 50: 2061–2070. https://doi.org/10.1109/JRPROC.1962.288235

7. Hodgkin AL, Huxley AF. A quantitative description of membrane current and its application to conduction and excitation in nerve. J Physiol. 1952; 117(4): 500–544. https://doi.org/10.1113/jphysiol.1952.sp004764

8. Van Capelle FJL, Durrer D. Computer simulation of arrhythmias in a network of coupled excitable elements. Circ Res. 1980; 47: 454–466. https://doi.org/10.1161/01.RES.47.3.454

9. Aliev RR, Panfilov AV. A simple two-variable model of cardiac excitation. Chaos Solitons Fractals. 1996; 7(3): 293–301. https://doi.org/10.1016/0960-0779(95)00089-5

10. Morris C, Lecar H. Voltage oscillations in the barnacle giant muscle fiber. Biophys J. 1981; 35: 193–213. https://doi.org/10.1113/jphysiol.1973.sp010146

11. Endresen LP. Chaos in weakly-coupled pacemaker cells. J Theor Biol. 1997; 184: 41–50. https://doi.org/10.1006/jtbi.1996.0240

12. González-Miranda JM. Nonlinear oscillations in a muscle pacemaker cell model. Commun Nonlinear Sci Numer Simul. 2017; 43: 330–340. https://doi.org/10.1016/j.cnsns.2016.07.018

13. Fenton F, Karma A. Vortex dynamics in three-dimensional continuous myocardium with fiber rotation: Filament instability and fibrillation. Chaos. 1998; 8(1): 20–47. https://doi.org/10.1063/1.166311

14. Mitchell CC, Schaeffer DG. A two-current model for the dynamics of cardiac membrane. Bull Mat Biol. 2003; 65: 767–793. https://doi.org/10.1016/S0092-8240(03)00041-7

15. Corrado C, Niederer SA. A two-variable model robust to pacemaker behaviour for the dynamics of the cardiac action potential. Math Biosci. 2016; 281: 46–54. https://doi.org/10.1016/j.mbs.2016.08.010

16. Plank G, Loewe A, Neic A, Augustin C, Huang Y-L, Gsell MAF, Karabelas E, Nothstein M, Prassl AJ, Sánchez J, Seemann G, Vigmond EJ. The openCARP simulation environment for cardiac electrophysiology. Comput Methods Programs Biomed. 2021; 208: 106223. https://doi.org/10.1016/j.cmpb.2021.106223 https://opencarp.org (2021).

17. Yu T, Lloyd CM, Nickerson DP, Cooling MT, Miller AK, Garny A, Terkildsen JR, Lawson J, Britten RD, Hunter PJ, Nielsen PM. The Physiome model repository 2. Bioinformatics 2011; 27: 743–744. Available from: https://models.physiomeproject.org/cellml https://doi.org/10.1093/bioinformatics/btq723

18. Gizzi A, Cherubini C, Migliori S, Alloni R, Portuesi R, Filippi S. On the electrical intestine turbulence induced by temperature changes. Phys Biol. 2010; 7: 16011. https://doi.org/10.1088/1478-3975/7/1/016011

19. Borek B, Shajahan TK, Gabriels J, Hodge A, Glass L, Shriera A. Pacemaker interactions induce reentrant wave dynamics in engineered cardiac culture. Chaos. 2012; 22: 033132. https://doi.org/10.1063/1.4747709

20. Podziemski P, Żebrowski JJ. Liénard-type models for the simulation of the action potential of cardiac nodal cells. Physica D. 2013; 261: 52–61. https://doi.org/10.1016/j.physd.2013.06.007

21. Ryzhii E, Ryzhii M. A heterogeneous coupled oscillator model for simulation of ECG signals. Comput Methods Programs Biomed. 2014; 117(1): 40–49. https://doi.org/10.1016/j.cmpb.2014.04.009

22. Li J, Inada S, Schneider JE, Zhang H, Dobrzynski H, Boyett MR. Three-dimensional computer model of the right atrium including the sinoatrial and atrioventricular nodes predicts classical nodal behaviours. PLoS ONE. 2014 Nov; 9(11): e112547. https://doi.org/10.1371/journal.pone.0112547

23. Izhikevich EM. Dynamical Systems in Neuroscience: The Geometry of Excitability and Bursting The MIT Press; 2006. https://doi.org/10.7551/mitpress/2526.001.0001

24. Corrado C, Whitaker J, Chubb H, Williams S, Wright M, Gill J, ONeill MD, Niederer SA. Personalized models of human atrial electrophysiology derived from endocardial electrograms. IEEE Trans Biomed Eng. 2017 Apr; 64(4): 735-742. https://doi.org/10.1109/TBME.2016.2574619. Epub 2016 May 30. PMID: 28207381.

25. Dhamala J, Arevalo HJ, Sapp J, Horácek BM, Wu KC, Trayanova NA, Wang L. Quantifying the uncertainty in model parameters using Gaussian process-based Markov chain Monte Carlo in cardiac electrophysiology. Med Image Anal. 2018; 48: 43–57. https://doi.org/10.1016/j.media.2018.05.007

26. Ravon G, Coudière Y, Potse M, Dubois R. Impact of the endocardium in a parameter optimization to solve the inverse problem of electrocardiography. Front Physiol. 2019; 9: 1946. https://doi.org/10.3389/fphys.2018.01946

27. Corrado C, Razeghi O, Roney C, Coveney S, Williams S, Sim I, O'Neill M, Wilkinson R, Oakley J, Clayton RH, Niederer S. Quantifying atrial anatomy uncertainty from clinical data and its impact on electro-physiology simulation predictions. Med Image Anal. 2020; 61: 101626. https://doi.org/10.1016/j.media.2019.101626

28. Teplenin AS, Dierckx H, de Vries AAF, Pijnappels DA, Panfilov AV. Paradoxical onset of arrhythmic waves from depolarized areas in cardiac tissue due to curvature-dependent instability. Phys Rev X. 2018; 8(2): 021077. https://doi.org/10.1103/PhysRevX.8.021077

29. Christoph J, Chebbok M, Richter C, Schröder-Schetelig J, Bittihn P, Stein S, Uzelac I, Fenton FH, Hasenfuß G, Gilmour Jr. RF, Luther S. Electromechanical vortex filaments during cardiac fibrillation. Nature. 2018; 555: 667–672. https://doi.org/10.1038/nature26001

30. Li T-C, Pan De-B, Zhou K, Jiang R, Jiang C, Zheng Bo, Zhang H. Jacobian-determinant method of identifying phase singularity during reentry. Phys Rev E. 2018; 98: 062405. https://doi.org/10.1103/PhysRevE.98.062405

31. Lebert J, Jan Christoph J. Synchronization-based reconstruction of electromechanical wave dynamics in elastic excitable media. Chaos. 2019; 29: 093117. https://doi.org/10.1063/1.5101041

32. Belhamadia Y, Grenier J. Modeling and simulation of hypothermia effects on cardiac electrical dynamics. PLoS ONE. 2019; 14(5): e0216058. https://doi.org/10.1371/journal.pone.0216058

https://10.1006/jtbi.2000.1069

33. Brandstaeter S, Gizzi A, Fuchs SL, Gebauer AM, Aydin RC, Cyron CJ. Computational model of gastric motility with active-strain electromechanics. ZAMM. 2018; 98: 2177–2197. https://doi.org/10.1002/zamm.201800166

34. Pullan AJ, Cheng LK, Yassi R, Buist ML. Modelling gastrointestinal bioelectric activity. Prog Biophys Mol Biol. 2004; 85: 523–550. https://doi.org/10.1016/j.pbiomolbio.2004.02.003

35. Sheldon RE, Baghdadi M, McCloskey C, Blanks AM, Shmygol A, van den Berg HA. Spatial heterogeneity enhances and modulates excitability in a mathematical model of the myometrium. J R Soc Interface. 2013; 10(86): 20130458. https://doi.org/10.1098/rsif.2013.0458

36. Seydewitz R, Menzel R, Siebert T, Böl M. Three-dimensional mechano-electrochemical model for smooth muscle contraction of the urinary bladder. J Mech Behav Biomed Mater. 2017; 75: 128–146. https://doi.org/10.1016/j.jmbbm.2017.03.034.

37. Fresca S, Manzoni A, Dedé L, Quarteroni A. Deep learning-based reduced order models in cardiac electrophysiology. PLoS ONE. 2020; 15(10): e0239416. https://doi.org/10.1371/journal.pone.0239416

38. Ai W, Patel ND, Roop PS, Malik A, Andalam S, Yip E, Allen N, Trew ML. Parametric computational model of the action potential of pacemaker cells. IEEE Trans Biomed Eng. 2018; 65(1): 123–130. https://doi.org/10.1109/TBME.2017.2695537

39. Sehgal S, Patel ND, Malik A, Roop PS, Trew ML. Resonant model - A new paradigm for modeling an action potential of biological cells. PLoS ONE. 2019; 14(5): e0216999. https://doi.org/10.1371/journal.pone.0216999

40. Keener J, Sneyd J. Mathematical Physiology I and II. Springer; 2009. https://doi.org/10.1007/978-0-387-75847-3 https://doi.org/10.1007/978-0-387-79388-7

41. Rabinovitch A, Aviram I, Gulko N, Ovsyshcher E. A model for the propagation of action potentials in non-uniformly excitable media. J Theor Biol. 1999; 196: 141–154. https://doi.org/10.1006/jtbi.1998.0824

42. Bracewell, R. Heaviside's unit step function, H(x). The Fourier transform and its applications 3rd ed. New York: McGraw-Hill; pp. 61-65, 2000.

43. Djabella K, Landau M, Sorine M. A two-variable model of cardiac action potential with controlled pacemaker activity and ionic current interpretation. In 46th IEEE Conference on Decision and Control. 2007; 5186–5191. https://doi.org/10.1109/CDC.2007.4434970

44. Ryzhii M, Ryzhii E. Simulation of ectopic activity onset in border zones between normal and damaged myocardium with minimal ionic models. In 2020 Computing in Cardiology (CinC). 2020; 9344249. https://doi.org/10.22489/CinC.2020.142

45. Kurata Y, Hisatome I, Imanishi S, Shibamoto T. Dynamical description of sinoatrial node pacemaking: improved mathematical model for primary pacemaker cell. Am J Physiol Heart Circ Physiol. 2002; 283(5): H2074–H2101. https://doi.org/10.1152/ajpheart.00900.2001

46. Li J, Zhang H, Boyett M. Numerical analysis of conduction of the action potential across the Purkinje fibre-ventricular muscle junction. In 2016 Computing in Cardiology Conference (CinC). 2016; 43: 265–268. https://doi.org/10.22489/CinC.2016.078-4192016

47. Li P, Lines GT, Maleckar MM, Tveito A. Mathematical models of cardiac pacemaking function. Front Phys. 2013; 1: 20. https://doi.org/10.3389/fphy.2013.00020

48. Oren RV, Clancy CE. Determinants of heterogeneity, excitation and conduction in the sinoatrial node: a model study. PLoS Comput Biol. 2010; 6(12): e1001041. https://doi: 10.1371/journal.pcbi.1001041.

49. Kharche SR, Vigmond E, Efimov IR, Dobrzynski H. Computational assessment of the functional role of sinoatrial node exit pathways in the human heart. PLoS ONE. 2017; 12(9): e0183727. https://doi.org/10.1371/journal.pone.0183727

50. Dhooge A, Govaerts W, Kuznetsov YuA, Meijer HGE, Sautois B. New features of the software MatCont for bifurcation analysis of dynamical systems. MCMDS 2008; 14(2): 147–175. https://doi.org/10.1080/13873950701742754

51. Clayton RH, Panfilov AV. A guide to modelling cardiac electrical activity in anatomically detailed ventricles. Prog. Biophys. Mol. Biol. 2008; 96: 19–43. https://doi:10.1016/j.pbiomolbio.2007.07.004

52. Ryzhii M, Ryzhii E. Development of simplified model of atrioventricular node with dual pathway. 2018 IEEE Int. Conf. on Bioinformatics and Biomedicine (BIBM). 2018; 2800–2802. https://doi.org/10.1109/BIBM.2018.8621149

53. Garny A, Kohl P, Hunter PJ, Boyett MR, Noble D. One-dimensional rabbit sinoatrial node models: benefits and limitations. J. Cardiovasc. Electrophysiol. 2003; 14(10 Suppl): S121–S132. https://doi.org/10.1046/j.1540.8167.90301.x.

54. Landau M, Lorente P, Henry J, Canu S. Hysteresis phenomena between periodic and stationary solutions in a model of pacemaker and nonpacemaker coupled cardiac cells. J Math Biol. 1987; 25: 491–509. https://doi.org/10.1007/BF00276195

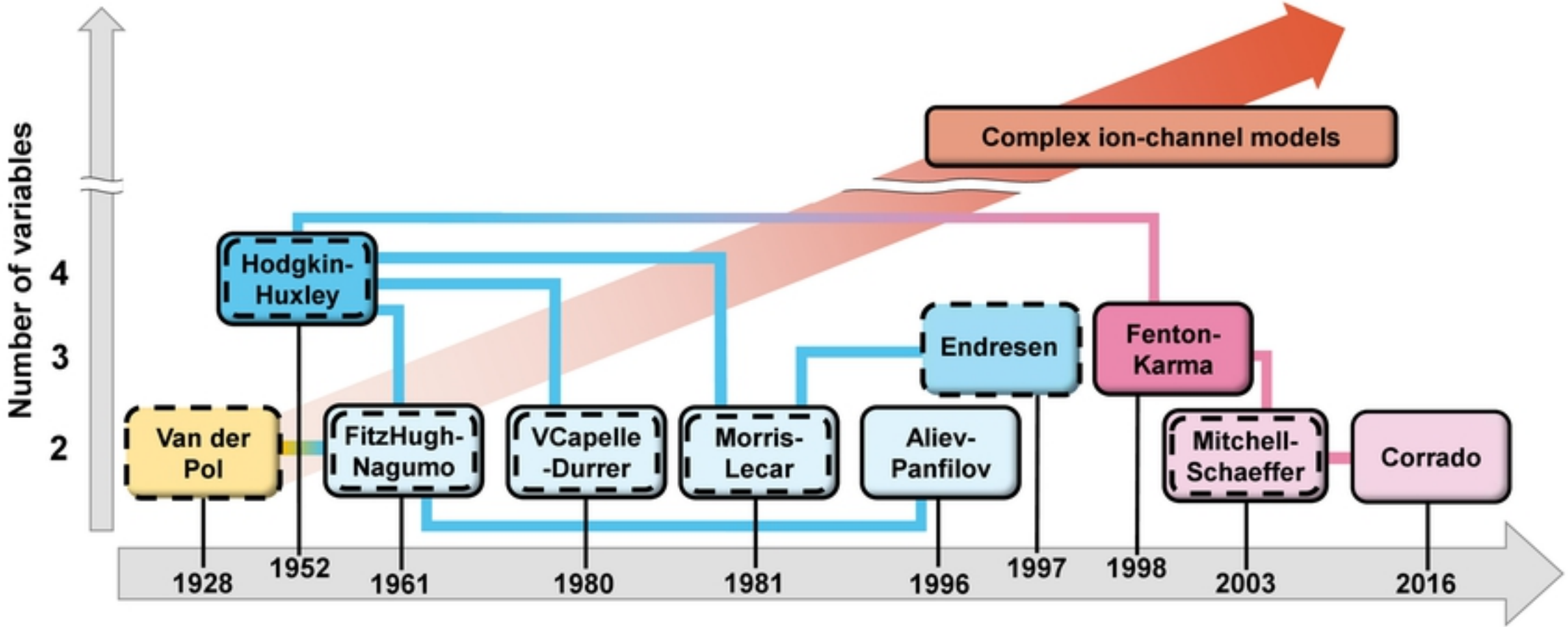
Complex ion-channel models
Number of variables
4
3
2
Hodgkin-Huxley
Van der Pol
FitzHugh-Nagumo
VCapelle-Durrer
Morris-Lecar
Aliev-Panfilov
Endresen
Fenton-Karma
Mitchell-Schaeffer
Corrado
1928
1952
1961
1980
1981
1996
1997
1998
2003
2016

Figure 1

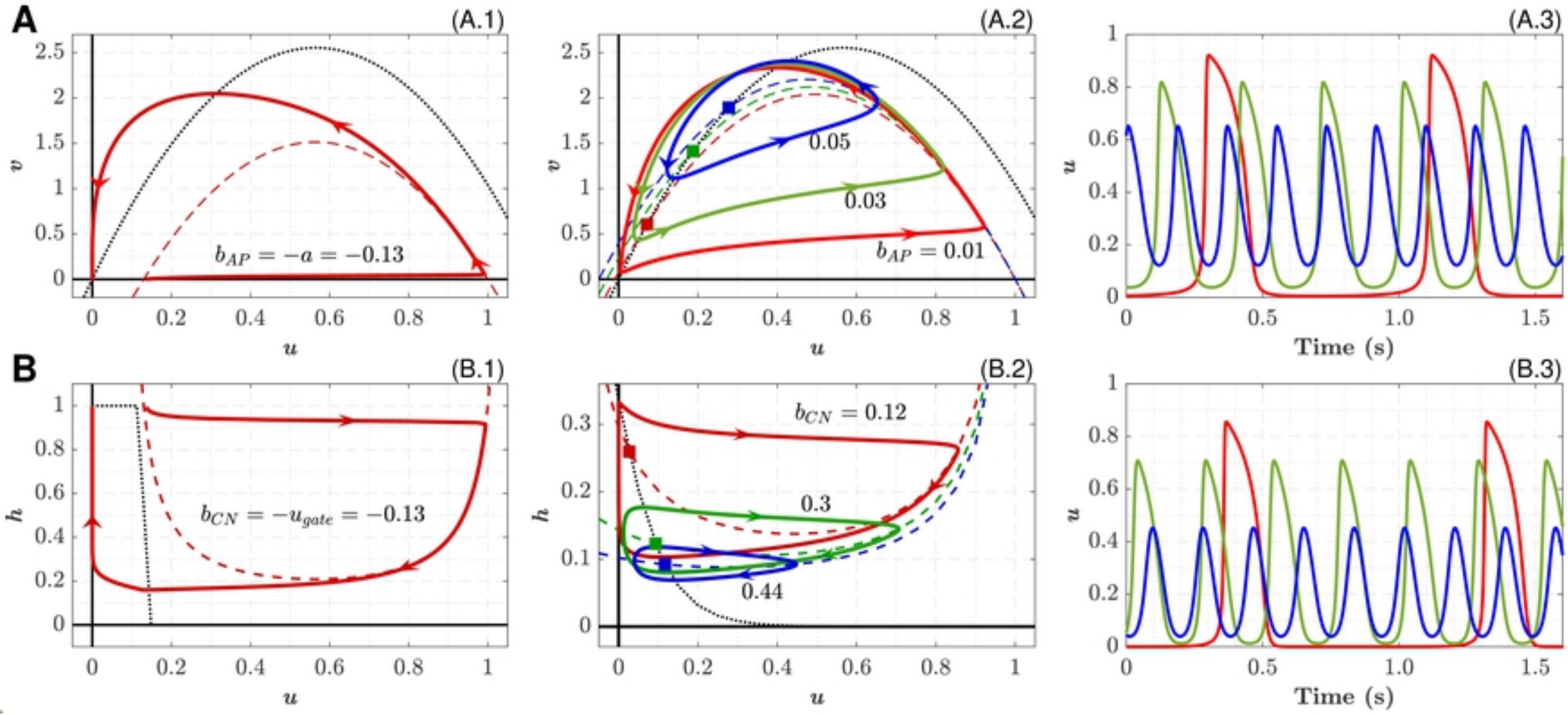
A
(A.1)
(A.2)
(A.3)
$b_{AP} = -a = -0.13$
0.05
0.03
$b_{AP} = 0.01$
B
(B.1)
(B.2)
(B.3)
$b_{CN} = -u_{gate} = -0.13$
$b_{CN} = 0.12$
0.3
0.44
Time (s)

Figure 2

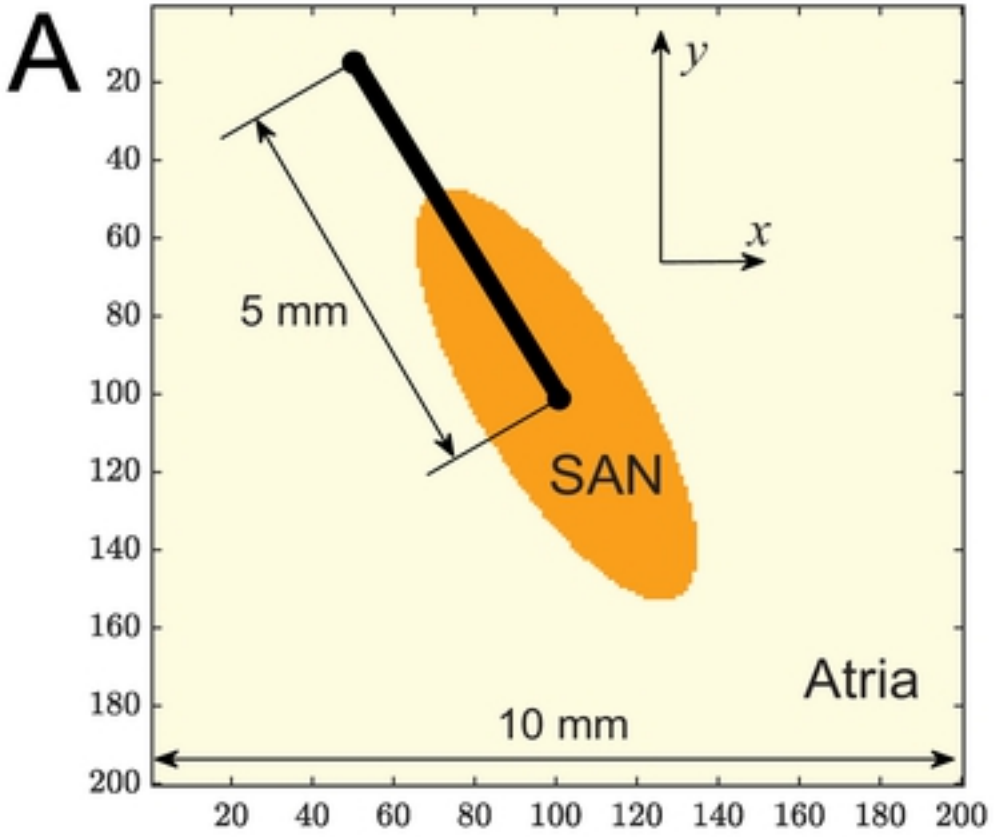
A
20
40
60
80
100
120
140
160
180
200
20
40
60
80
100
120
140
160
180
200
y
x
5 mm
SAN
Atria
10 mm

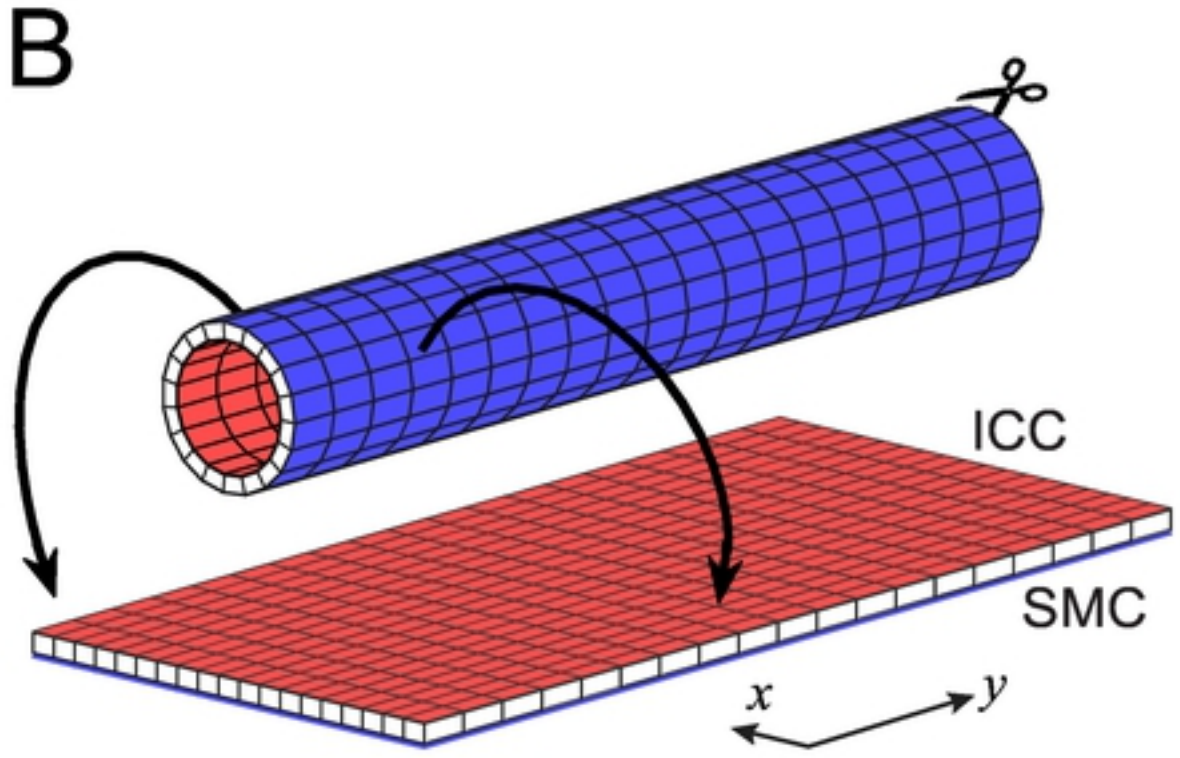
B
ICC
SMC
x
y

Figure 3

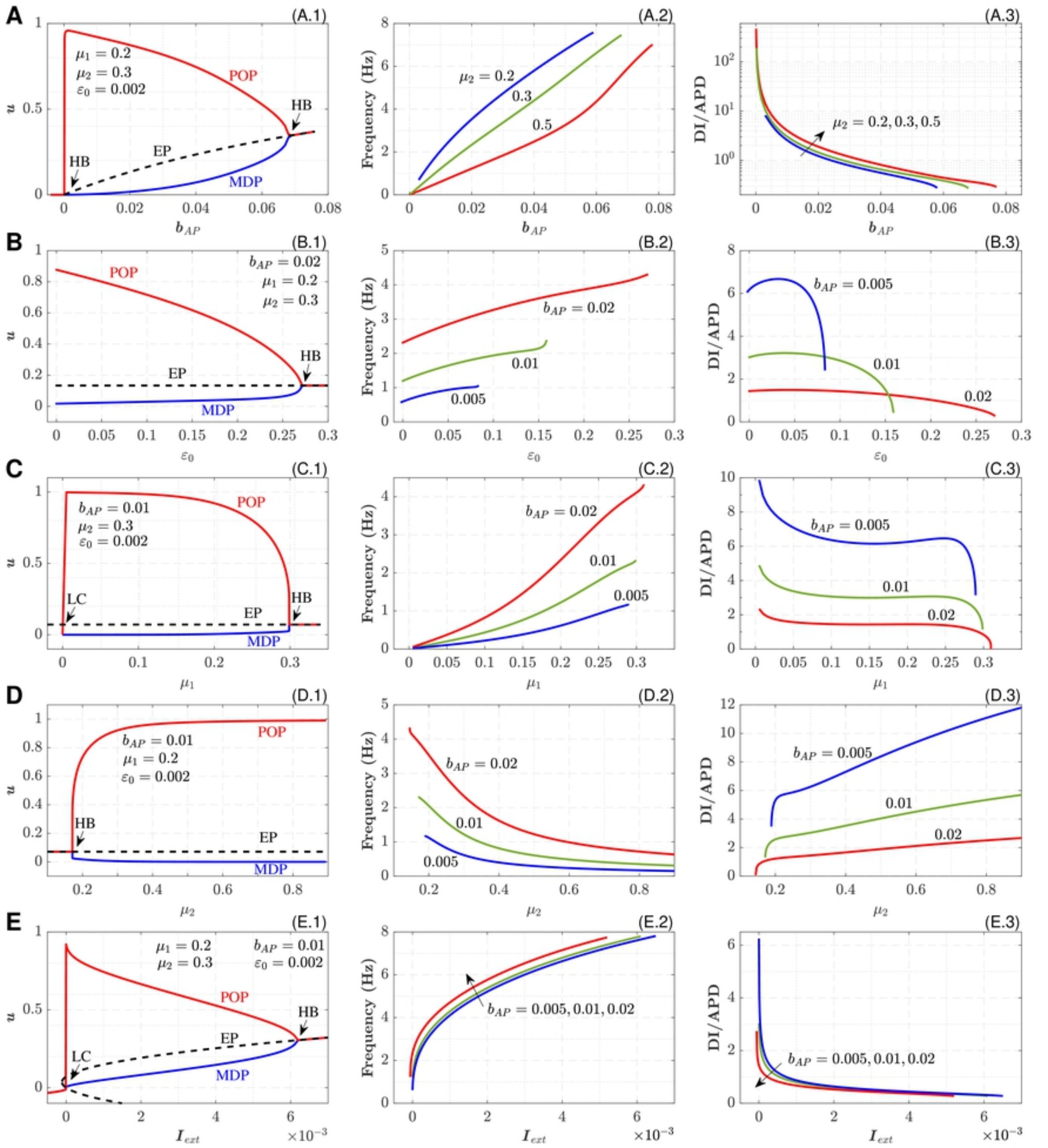
A
(A.1)
$\mu_1 = 0.2$
$\mu_2 = 0.3$
$\varepsilon_0 = 0.002$
POP
HB
EP
HB
MDP
u
b_{AP}
(A.2)
$\mu_2 = 0.2$
0.3
0.5
Frequency (Hz)
b_{AP}
(A.3)
$\mu_2 = 0.2, 0.3, 0.5$
DI/APD
b_{AP}
B
(B.1)
$b_{AP} = 0.02$
$\mu_1 = 0.2$
$\mu_2 = 0.3$
POP
HB
EP
MDP
u
ε_0
(B.2)
$b_{AP} = 0.02$
0.01
0.005
Frequency (Hz)
ε_0
(B.3)
$b_{AP} = 0.005$
0.01
0.02
DI/APD
ε_0
C
(C.1)
$b_{AP} = 0.01$
$\mu_2 = 0.3$
$\varepsilon_0 = 0.002$
POP
LC
EP
HB
MDP
u
μ_1
(C.2)
$b_{AP} = 0.02$
0.01
0.005
Frequency (Hz)
μ_1
(C.3)
$b_{AP} = 0.005$
0.01
0.02
DI/APD
μ_1
D
(D.1)
$b_{AP} = 0.01$
$\mu_1 = 0.2$
$\varepsilon_0 = 0.002$
POP
HB
EP
MDP
u
μ_2
(D.2)
$b_{AP} = 0.02$
0.01
0.005
Frequency (Hz)
μ_2
(D.3)
$b_{AP} = 0.005$
0.01
0.02
DI/APD
μ_2
E
(E.1)
$\mu_1 = 0.2$
$\mu_2 = 0.3$
$b_{AP} = 0.01$
$\varepsilon_0 = 0.002$
POP
HB
EP
LC
MDP
u
I_{ext}
$\times 10^{-3}$
(E.2)
$b_{AP} = 0.005, 0.01, 0.02$
Frequency (Hz)
I_{ext}
$\times 10^{-3}$
(E.3)
$b_{AP} = 0.005, 0.01, 0.02$
DI/APD
I_{ext}
$\times 10^{-3}$

Figure 4

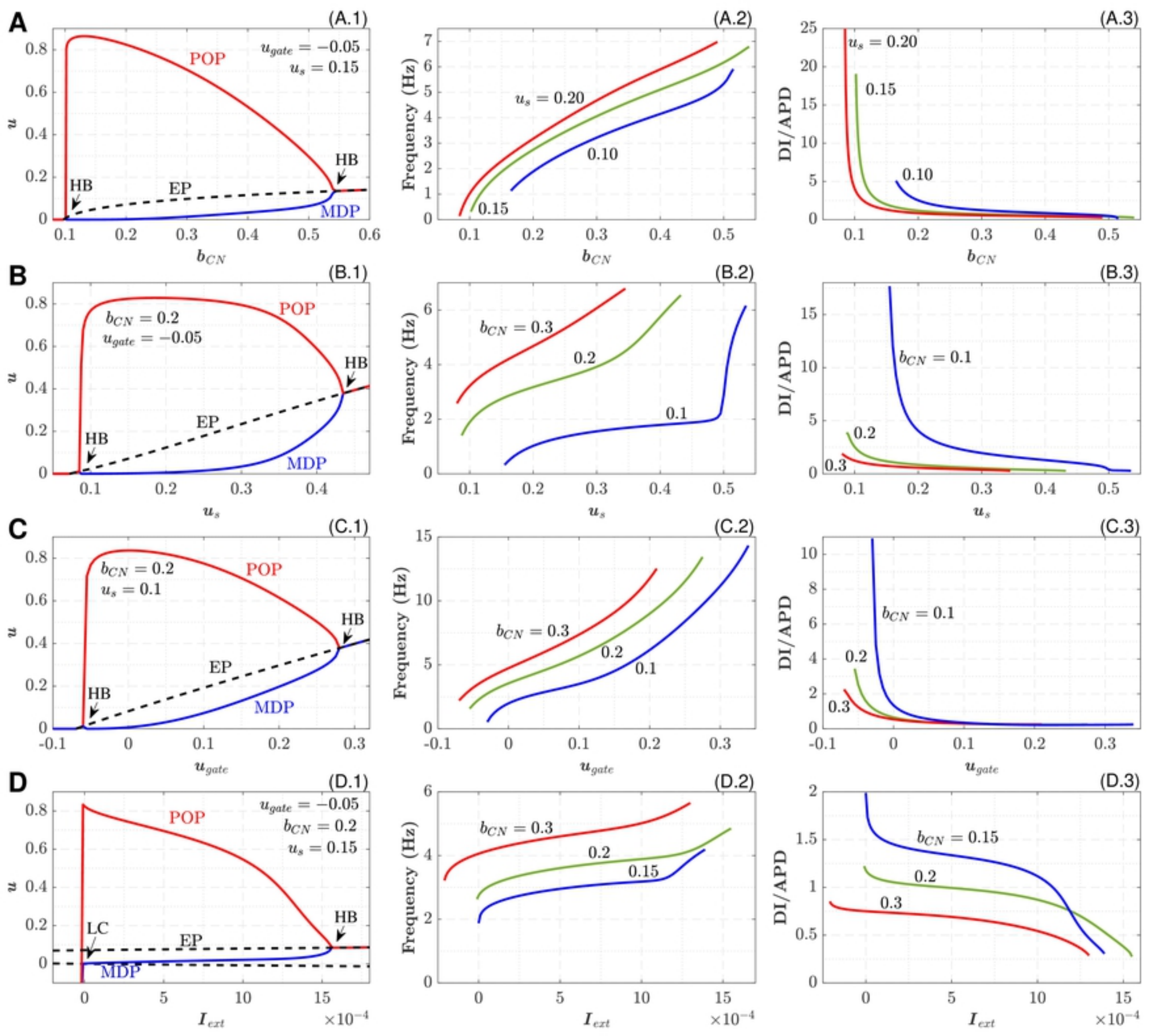
A
(A.1)
$u_{gate} = -0.05$
$u_s = 0.15$
POP
HB
EP
MDP
u
b_{CN}
(A.2)
Frequency (Hz)
$u_s = 0.20$
0.10
0.15
b_{CN}
(A.3)
DI/APD
$u_s = 0.20$
0.15
0.10
b_{CN}
B
(B.1)
$b_{CN} = 0.2$
$u_{gate} = -0.05$
POP
HB
EP
MDP
u
u_s
(B.2)
Frequency (Hz)
$b_{CN} = 0.3$
0.2
0.1
u_s
(B.3)
DI/APD
$b_{CN} = 0.1$
0.2
0.3
u_s
C
(C.1)
$b_{CN} = 0.2$
$u_s = 0.1$
POP
HB
EP
MDP
u
u_{gate}
(C.2)
Frequency (Hz)
$b_{CN} = 0.3$
0.2
0.1
u_{gate}
(C.3)
DI/APD
$b_{CN} = 0.1$
0.2
0.3
u_{gate}
D
(D.1)
$u_{gate} = -0.05$
$b_{CN} = 0.2$
$u_s = 0.15$
POP
LC
EP
HB
MDP
u
I_{ext}
$\times 10^{-4}$
(D.2)
Frequency (Hz)
$b_{CN} = 0.3$
0.2
0.15
I_{ext}
$\times 10^{-4}$
(D.3)
DI/APD
$b_{CN} = 0.15$
0.2
0.3
I_{ext}
$\times 10^{-4}$

Figure 5

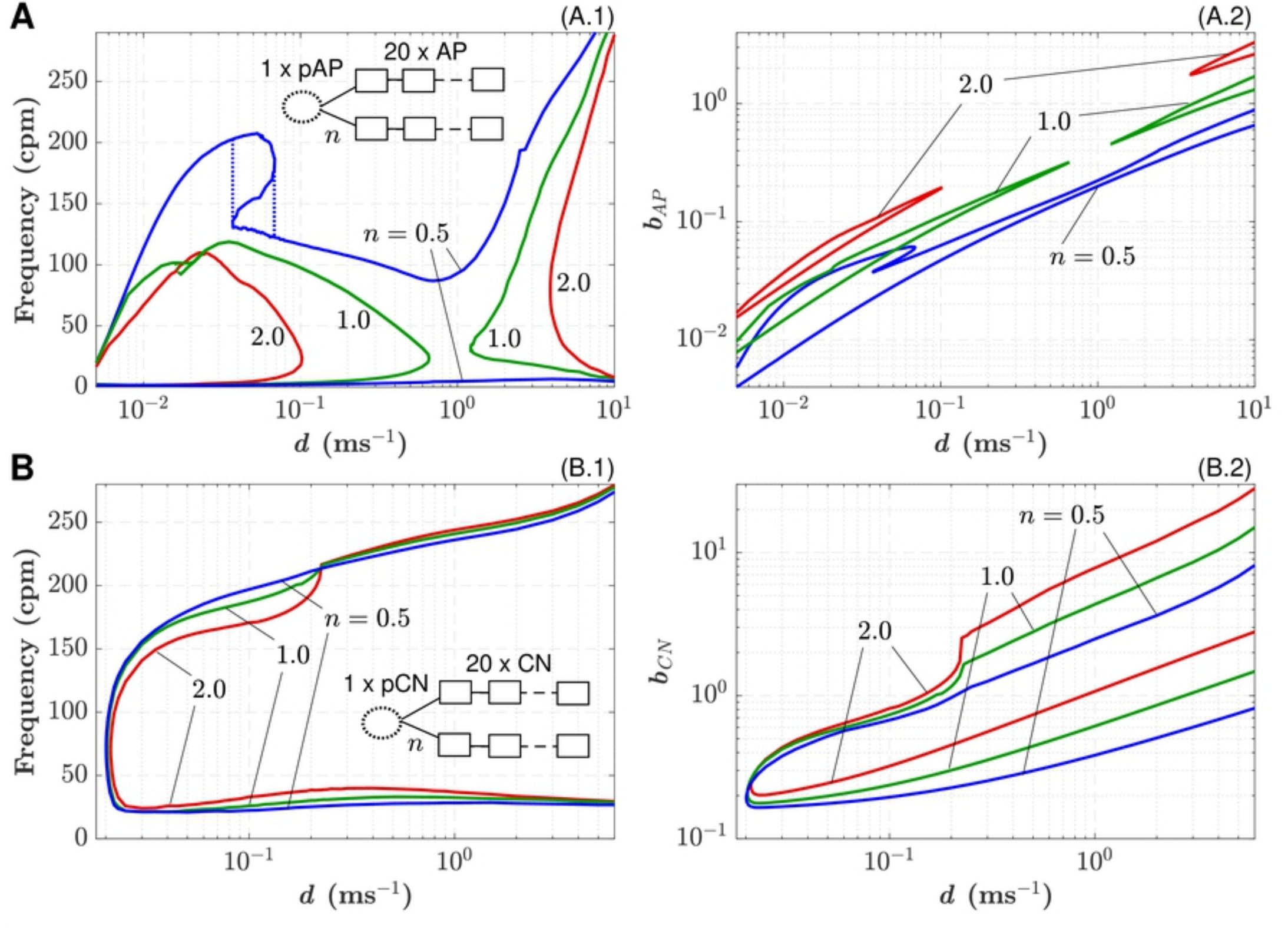
A
(A.1)
(A.2)
1 x pAP
20 x AP
n
n = 0.5
2.0
1.0
Frequency (cpm)
d (ms⁻¹)
b_AP
B
(B.1)
(B.2)
1 x pCN
20 x CN
b_CN

Figure 6

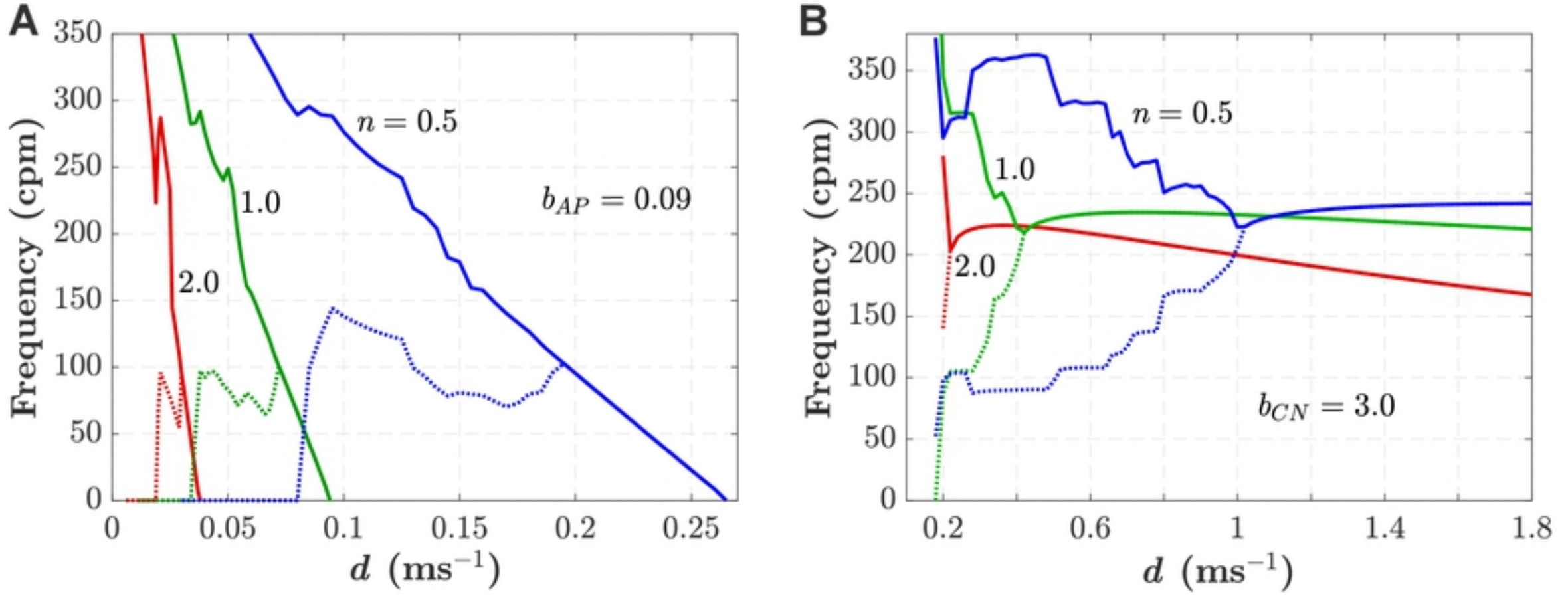

Figure 7

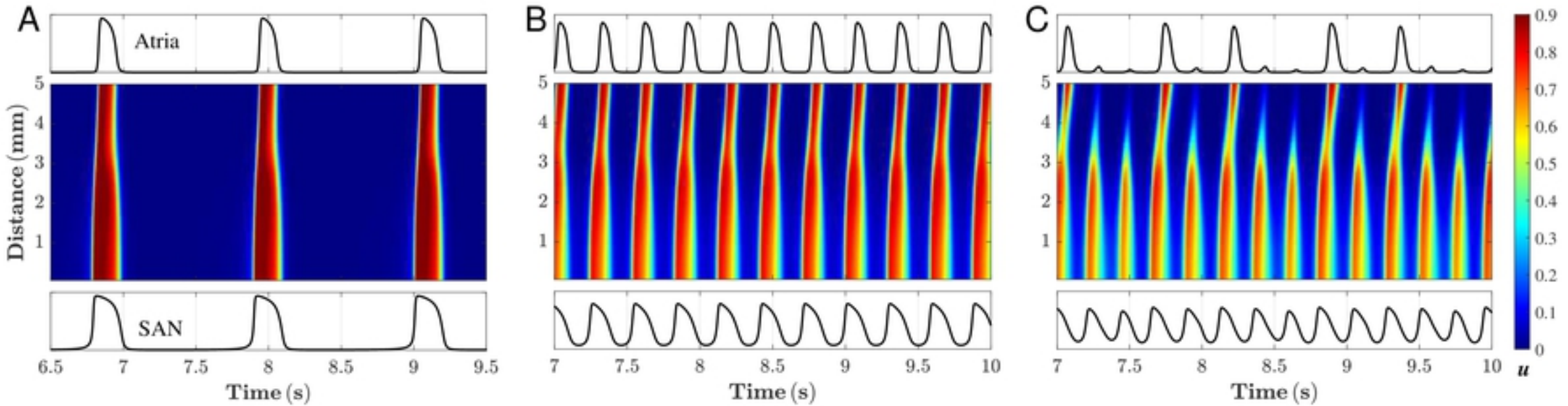

Figure 8

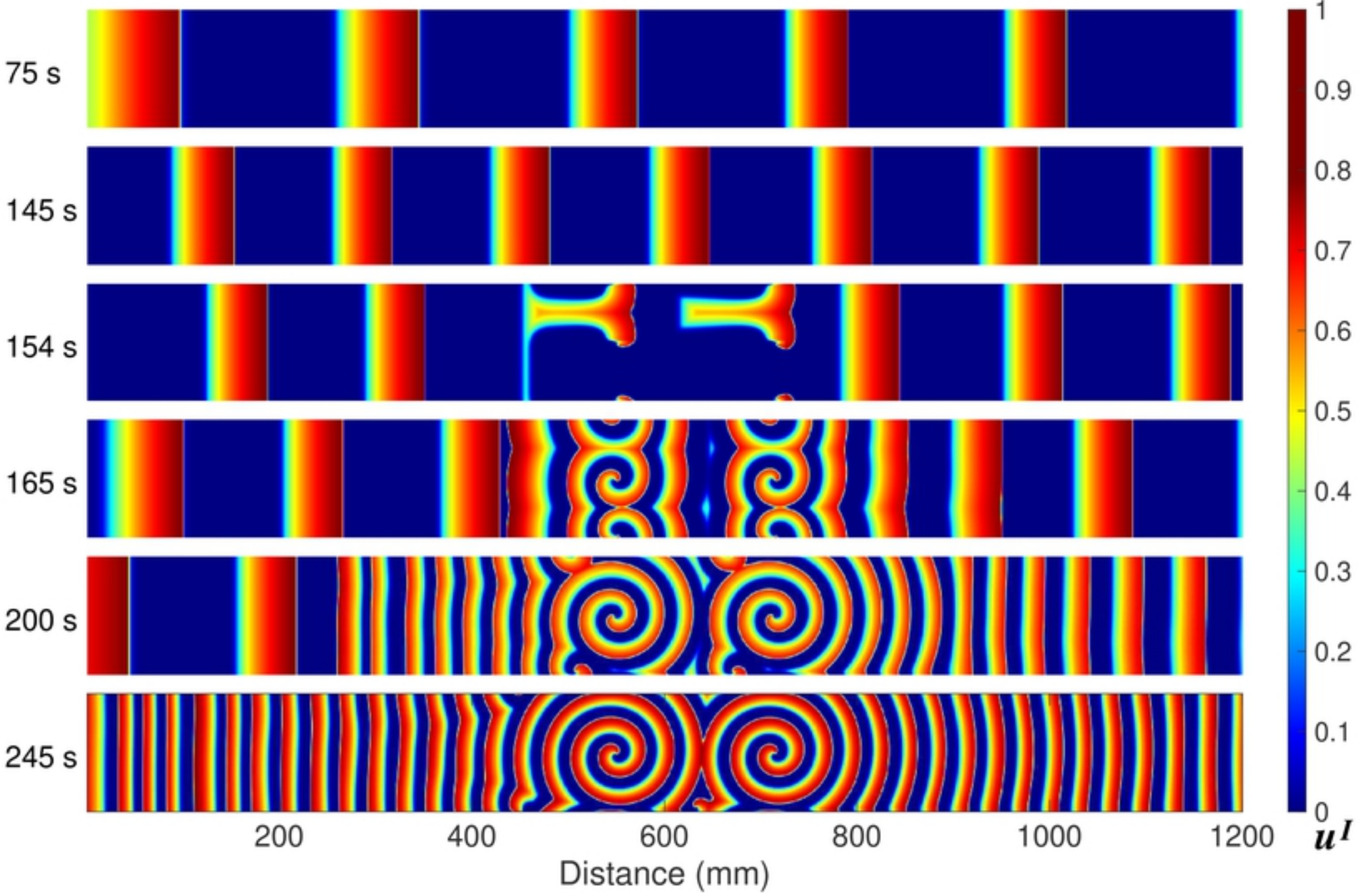
75 s
145 s
154 s
165 s
200 s
245 s
200
400
600
800
1000
1200
Distance (mm)
1
0.9
0.8
0.7
0.6
0.5
0.4
0.3
0.2
0.1
0
u^I

Figure 9